PHYSICAL REVIEW A **102**, 063503 (2020)

Non-Hermitian analysis of surface creeping waves in optical microcavities: Nature of external resonances

Chang-Hwan Yi,* Hyeon-Hye Yu, and Chil-Min Kim
Department of Emerging Materials Science, DGIST, Daegu 42988, Republic of Korea

(Received 17 May 2020; accepted 17 November 2020; published 3 December 2020)

Undiscovered properties of surface creeping wave states given by complex angular momentum poles, so-called Regge poles (RPs) in optical microcavity scattering, are transparently elucidated on the frameworks of non-Hermitian physics. In particular, we analytically show that the nature of external resonances (ERs) given by complex wave numbers is equivalent to surface creeping wave RPs. Moreover, by obtaining the full structural characteristics of RPs for different polarizations, it is found that notable nontrivial RPs in transverse-magnetic polarization arise owing to the classical Brewster angle. Finally, we explicitly demonstrate the emergence of non-Hermitian degeneracies incorporating different classes of RPs.

DOI: 10.1103/PhysRevA.102.063503

I. INTRODUCTION

Non-Hermitian physics is one of the active research fields today, as generic realistic physical systems are open systems [1–5]. Under the canonical Sommerfeld radiation condition [6], this openness gives rise to decaying states described in terms of complex-valued eigenvalues. These conventional states are dominantly confined inside the system and are referred to as internal resonances (IRs). Up to date, they have been widely proven to form non-Hermitian degeneracies, so-called exceptional points (EPs) [7–16], at which eigenvalues, as well as corresponding eigenstates, coalesce simultaneously. Besides these traditional IRs, recently, another exotic class of resonances, so-called external resonances (ERs), was discovered in optical systems [17–19]. More strikingly, it was shown that IRs and ERs can merge to form EPs as well [19].

In contrast to IRs, very little is known about ERs; particularly, their physical substantiation is still controversial, since their wave functions almost vanish inside the system and quickly diverge outside the system. This extreme divergence in space is, however, an artificial consequence of a rapid exponential decay of waves in time [20,21], which can be interpreted as a retardation effect [20]; waves, $\psi(t,r) \sim e^{ik_r r}e^{k_i r}e^{-i\omega_r t}e^{-\omega_i t}$, fulfilling the Sommerfeld radiation condition, spatially diverge when $r \to \infty$ and temporally converge to zero when $t \to \infty$, since $\omega = ck \iff \omega_r + i\omega_i = c(k_r + ik_i)$, where $\{\omega_r, \omega_i, k_r, k_i\} \in \mathbb{R}^+$, $i = \sqrt{-1}$, and c is the speed of light. Because of those inherent ambiguities, ERs have been underestimated significantly more than they deserve, even after the interactions between IRs and ERs were explicitly clarified [18,19]. Working out these unresolved questions in depth, in this paper we will show that the nature of ERs is the surface creeping wave, which is accessible by employing the complex angular momentum (CAM) of the Sommerfeld-Watson transformation [22–26]. In the course of demonstrations, profound structural properties of CAMs, as well as the emergence of EPs of CAMs, will be unveiled.

Complex angular momentum poles of a scattering matrix [27–29] are essentially equivalent to the familiar energetic poles and are called Regge poles (RPs) [30–33]. The energy-dependent variations of RPs are referred to as Regge trajectories (RTs) [34]. Because CAMs have not been well explored from the viewpoint of non-Hermitian physics, many faces of their intrinsic characteristics in this aspect are still not well understood. Originally, the CAM approach was proposed to overcome the slow convergence of the partial-wave sums given by a Mie series [27–29] for creeping microwaves around the Earth [35]. So far, the CAM technique has been successfully applied to a great variety of research fields, such as electromagnetic waves [36,37], quantum field theories [38,39], acoustics [40–42], black hole and gravitational waves [43–46], surface polaritons [47,48], fundamental particle waves [49,50], and Aharonov-Bohm effects [51]. Alongside these foundational topics, there are fresh trials to use CAMs for communication signals of wearable devices around a human body [52] or the remote sensing of target objects [53].

II. PRINCIPLES OF SCATTERING AND RESONANCE

We first begin with discussions of the ordinary scattering of a two-dimensional optical microdisk excited by an incident plane wave. As shown in Fig. 1, general incident fields result in reflection, transmission, and creeping surface waves. Moreover, since the size of our microdisk is in the Mie regime, forward scattering is dominant. Assuming time harmonics, $e^{-i\omega t}$, we solve the time-independent wave equation $-\nabla^2\psi = n(\vec{r})^2k^2\psi$ for optical fields, where $k = k_r - ik_i$ is the vacuum wave number for $\{k_r, k_i\} \in \mathbb{R}^+$, and $n(\vec{r})$ the position-dependent refractive index. Here, k_r and k_i correspond to the frequency and the decay rate of fields, respectively. From now on, a dimensionless wave number kR scaled by a disk radius R is used.

*yichanghwan@hanmail.net

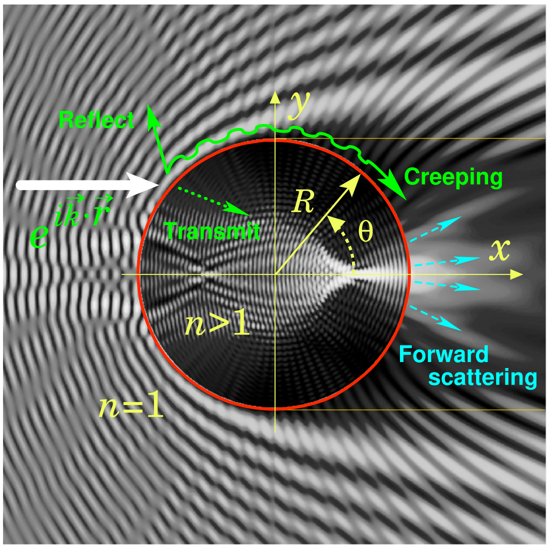

FIG. 1. A schematic of plane-wave scattering impacting on a dielectric disk with a wave number $kR \approx 44$ and an impinging angle $\theta = 0$. In this illustration, a refractive index is set to be $n = 2.4$ inside the disk, $r < R$, and $n = 1$ otherwise. A geometric optically inaccessible shadow region is in between the two horizontal straight lines.

By means of a Jacobi-Anger expansion [27–29], optical fields in and outside of a microdisk can be given by partial-wave sums as follows:

$$\psi_{r<R}(r,\theta) = \sum_{m=-\infty}^{\infty} i^m A_m J_m(nkr)e^{im\theta},$$
$$\psi_{r>R}(r,\theta) = \sum_{m=-\infty}^{\infty} i^m \big[J_m(kr) + S_m H_m^{(1)}(kr)\big]e^{im\theta}, \quad (1)$$

where J_m, $H_m^{(1)}$, A_m, and S_m are the mth-order Bessel function of the first kind, the Hankel function of the first kind, a transmission coefficient, and a scattering coefficient, respectively. For the regularity of the transmitted fields at the origin $r = 0$, only J_m is taken for $r < R$. Imposing the dielectric boundary condition at the disk boundary $r = R$ for $\theta \in [0, 2\pi)$,

$$\partial_\alpha \psi_{r<R}(R) = \mathcal{N}^2 \partial_\alpha \psi_{r>R}(R) \quad \text{and} \quad \psi_{r<R}(R) = \psi_{r>R}(R),$$

we can fix the coefficients A_m and S_m as follows:

$$A_m = \frac{2i/(\pi kR)}{J_m(nkR)H_m'^{(1)}(kR) - \mathcal{N}J_m'(nkR)H_m^{(1)}(kR)},$$
$$S_m = -\frac{J_m(nkR)J_m'(kR) - \mathcal{N}J_m'(nkR)J_m(kR)}{J_m(nkR)H_m'^{(1)}(kR) - \mathcal{N}J_m'(nkR)H_m^{(1)}(kR)}. \quad (2)$$

Here, $\partial_\alpha \equiv \vec{\alpha}\cdot\vec{\nabla}$, and $\vec{\alpha}$ is an outward-unit normal vector of the disk boundary. The prefactor $\mathcal{N}$ is selected according to the field polarization: $\mathcal{N} = n$ for transverse magnetic [TM: $\psi = (0, 0, E_z)$] polarization and $\mathcal{N} = 1/n$ for transverse electric [TE: $\psi = (0, 0, H_z)$] polarization.

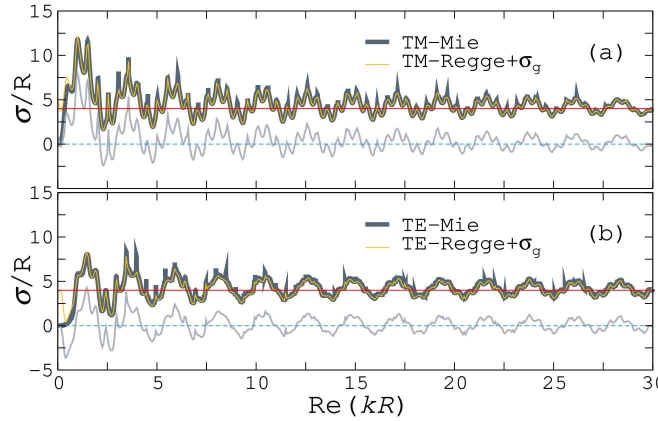

FIG. 2. Total scattering cross section as a function of kR for (a) TM and (b) TE polarization obtained by Mie sums (thick black) and by RPs (thin orange) for $n = 2.4$. The thin gray oscillating curves around $\sigma/R = 0$ represent the RP contributions only. The thin red lines at $\sigma/R = 4$ stand for the background integral contribution $\sigma_g/R = 4$ (see text).

Having computed the scattering coefficient S_m, we can deduce the scattering amplitude,

$$f(\theta, kR) = \frac{1-i}{\sqrt{\pi kR}} \sum_{m=-\infty}^{\infty} S_m(kR)e^{im\theta}, \quad (3)$$

by comparing the asymptotic far fields,

$$\psi(r,\theta) = \psi_{\text{incident}} + \psi_{\text{scattered}} \sim e^{i\vec{k}\cdot\vec{r}} + f(\theta, kR)\frac{e^{ikr}}{\sqrt{r}},$$

to Eqs. (1) with $H_m^{(1)}(kr) \approx (1-i)/\sqrt{\pi k}(-i)^m e^{ikr}/\sqrt{r}$ for $r \to \infty$. Given the scattering amplitude, the total scattering cross section,

$$\sigma/R = \int_0^{2\pi} |f(\theta, kR)|^2 d\theta = \frac{4}{kR}\sum_{m=-\infty}^{\infty} |S_m(kR)|^2, \quad (4)$$

can be obtained, as shown in Fig. 2. In the figure, we can identify the characteristic structures of sharp peaks imprinted on the bold fluctuations that are induced by resonances corresponding to poles of $S_m(kR)$ such that

$$J_m(nkR)H_m'^{(1)}(kR) = \mathcal{N}J_m'(nkR)H_m^{(1)}(kR). \quad (5)$$

Resonances $kR \in \mathbb{C}$ as solutions of Eq. (5) are located in the fourth quadrant, $\{\mathrm{Re}(kR) > 0, \mathrm{Im}(kR) < 0\}$, and are classified into two groups [17–19,36,37]: IRs for $|\mathrm{Re}(kR)| \gg |\mathrm{Im}(kR)|$ and ERs for $|\mathrm{Re}(kR)| \lesssim |\mathrm{Im}(kR)|$. In Fig. 3, we can clearly discern ERs from IRs by their considerably larger values of $|\mathrm{Im}(kR)|$ than those of IRs. Note that in quantum mechanical terminologies, IRs and ERs are called Fashbach and shape resonances [54,55], respectively.

III. SURFACE CREEPING WAVES: NATURE OF EXTERNAL RESONANCE

In this section, we demonstrate the fact that the nature of ER in optical microdisks is the surface creeping wave. To this end, we construct asymptotic (i.e., $|kR| \gg 1$) kR's for ERs expressed in terms of angular momentum m. This

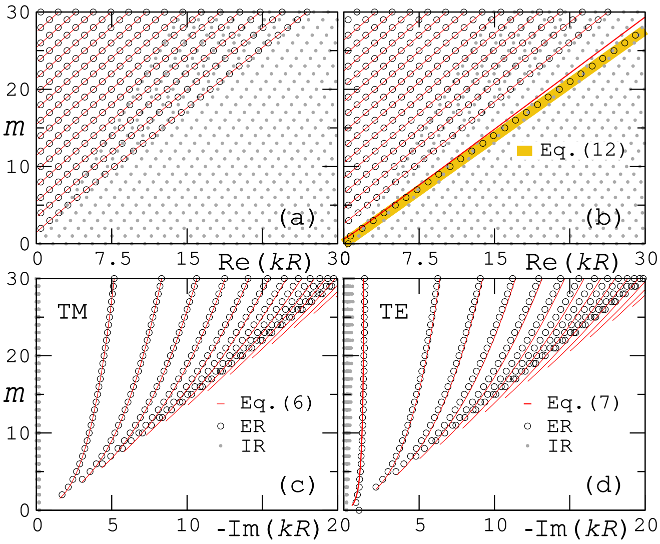

FIG. 3. Wave numbers as solutions of Eq. (5) for integer values of m with $n = 2.4$. (a) Real and (c) imaginary parts of wave numbers for TM polarization, and (b), (d) for TE polarization. Solid dots (•) and open circles (○) mark the internal and external resonances. Thin solid curves are the asymptotic results of Eq. (6) for the TM case and of Eq. (7) for the TE cases. The thick solid curve in (b) represents the Brewster modes of Eq. (12).

can be achieved perturbatively from the poles of the perfect-electric-conductor (PEC) scattering that are well interpreted as creeping waves [27–29,56–58].

The poles of the PEC scattering obey the Dirichlet boundary condition $[H_m^{(1)}(k_{\mathrm{PEC}}^{\mathrm{TM}}R) = 0]$ for TM and the Neumann boundary condition $[H_m'^{(1)}(k_{\mathrm{PEC}}^{\mathrm{TE}}R) = 0]$ for TE polarization, respectively. Now, suppose that kR's of Eq. (5) for TM are at the vicinity of $k_{\mathrm{PEC}}^{\mathrm{TM}}R$ such that $kR \to k_{\mathrm{PEC}}^{\mathrm{TM}}R + \delta$ for $|\delta| \ll |k_{\mathrm{PEC}}^{\mathrm{TM}}R|$, then the asymptotic kR's can read [54]

$$k_{l,m}^{\mathrm{ER\text{-}TM}}R \approx k_{\mathrm{PEC}}^{\mathrm{TM}}R + \delta \approx m + \alpha_l m^{\frac{1}{3}} + \beta_l m^{-\frac{1}{3}} - \frac{i}{\sqrt{n^2-1}} + \frac{i\alpha_l m^{-\frac{2}{3}}}{3(n^2-1)^{\frac{3}{2}}} \quad (n > 1), \tag{6}$$

with $J_m'(z)/J_m(z) \approx i\sqrt{1 - m^2/z^2}$ [24–26]. Here, $\alpha_l = 2^{-1/3}e^{-i2\pi/3}\kappa_l$, $\beta = 2^{-2/3}e^{-i4\pi/3}3\kappa_l^2/10$, and $-\kappa_l$ is the lth zeros of the Airy function of the first kind, i.e., $\mathrm{Ai}(-\kappa_l) = 0$ [59]. It is emphasized that although Ref. [54] claimed that Eq. (6) is applicable to the TE case too, actually, it is valid for the TM case only. Instead, the correct asymptotic kR's for TE polarization can be obtained near $k_{\mathrm{PEC}}^{\mathrm{TE}}R$ of the PEC scattering, obeying the Neumann boundary condition by means of the similar procedures implemented in Ref. [54], as follows:

$$\begin{aligned} k_{l,m}^{\mathrm{ER\text{-}TE}}R &\approx k_{\mathrm{TE}}^{\mathrm{PEC}}R + \bar{\delta} \approx m + \bar{\alpha}_l m^{\frac{1}{3}} + \bar{\beta}_l m^{-\frac{1}{3}} \\ &\quad + \frac{i\left[\bar{\alpha}_l^2(1-3n^2) + 2\bar{\beta}_l(n^2-1)\right]}{4\bar{\alpha}_l^2 n^2(n^2-1)} - \frac{i\sqrt{n^2-1}}{2\bar{\alpha}_l n^2 m^{-\frac{2}{3}}} \\ &\quad - \frac{i\left[(n^2-1)^2\left(3\bar{\alpha}_l^2 - 2\bar{\beta}_l\right)^2 - 2\bar{\alpha}_l^4\right]}{8\bar{\alpha}_l^3 n^2(n^2-1)^{\frac{3}{2}} m^{\frac{2}{3}}} \quad (n > 1), \end{aligned} \tag{7}$$

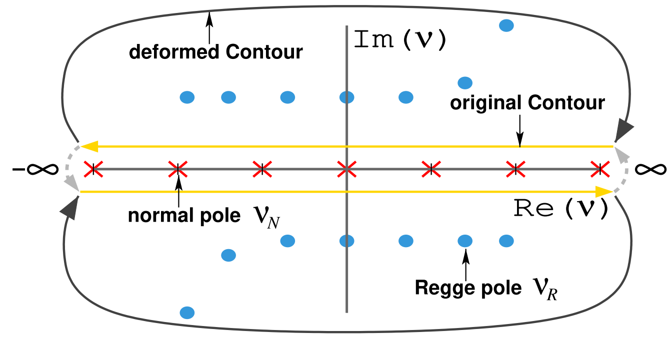

FIG. 4. Schematic illustration of the integral contours. For the integral of Watson transformation in Eq. (9), the original contour enclosing normal poles $\{\times; \nu_N \in \mathbb{Z}\}$ is deformed to enclose the Regge poles $\{\bullet; \nu_R \in \mathbb{C}\}$ in the sense of Cauchy's residue theorem.

where $\bar{\alpha}_l = 2^{-1/3}e^{-i2\pi/3}\bar{\kappa}_l$, $\bar{\beta}_l = (\bar{\kappa}_l^2 3/10 - \bar{\kappa}_l/5)2^{-2/3} e^{-i4\pi/3}$ [59], and $-\bar{\kappa}_l$ is the lth zeros of the derivative of the Airy function of the first kind, i.e., $\mathrm{Ai}'(-\bar{\kappa}_l) = 0$.

In Fig. 3, a definite agreement between the direct numerical solutions of Eq. (5) (open circles) and the results of Eqs. (6) and (7) (thin solid curves) is well proved. Each of the first three terms on the right-hand side (RHS) in Eqs. (6) and (7) are the same ones that correspond to the creeping wave modes in PEC scattering, whereas the remaining terms are the dielectric corrections. In-depth detailed explanations associated with this dielectric correction can be found, e.g., in Ref. [25]. Because this dielectric correction arises due to the wave transmission toward the inside of the optical microcavity from the surface, it disappears as $n \to \infty$. Therefore, it is consistent with the results of Ref. [17]: ERs converge to zeros of $H_m(z)$ for TM polarization and to those of $H_m'(z)$ for TE polarization, respectively. Note that Eqs. (6) and (7) are valid when the refractive index is not too close to unity and fail in the limit $n \to 1$.

IV. POLARIZATION-DEPENDENT REGGE POLES AND REGGE TRAJECTORIES

Now, we explicitly calculate the creeping wave RPs corresponding to $k_{l,m}^{\mathrm{ER}}R$. Applying the Sommerfeld-Watson series-to-integral transformation [27–29]

$$\sum_{m=-\infty}^{\infty} g(m) = \frac{1}{2\pi i}\oint_C \frac{\pi g(\nu)e^{-i\nu\pi}}{\sin(\nu\pi)}d\nu \tag{8}$$

to Eq. (3), we obtain the integral representation of the scattering amplitude as

$$f(\theta, kR) = -\frac{i+1}{2\sqrt{\pi kR}}\oint_C \frac{S_\nu(kR)e^{i\nu(\theta-\pi)}}{\sin(\nu\pi)}d\nu. \tag{9}$$

The contour C encloses the normal poles: $\nu_N \in \mathbb{Z}$ of $\sin(\nu_N\pi) = 0$ on the real axis, and it is easy to recover the original Mie series sum in Eq. (3) by the residue theorem [60], taking these poles into account. In Fig. 4, we can see the positions of the normal poles and the contour of the integral enclosing these poles. The integrand in Eq. (9) has another family of singularities [30–32]: $\nu_R \in \mathbb{C}$ satisfying Eq. (5), i.e.,

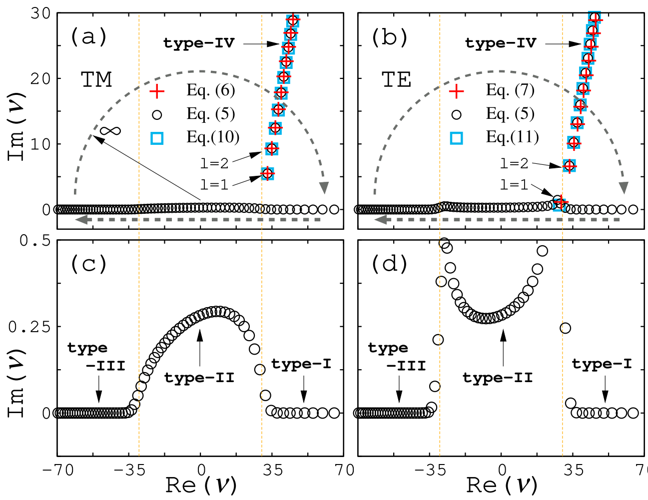

FIG. 5. RPs for TM [(a), (c)] and TE [(b), (d)] polarization on the upper-half CAM plane, $[\mathrm{Re}(\nu), \mathrm{Im}(\nu)]$, at $\mathrm{Re}(kR) = 30$. Open circles ($\circ$) mark the poles obtained numerically by Eq. (5), crosses (+) Eqs. (6) and (7), and squares ($\square$) Eqs. (10) and (11), respectively. Gray dashed arrowed curves in (a) and (b) are the schematic representations of the deformed integral contour enclosing RPs (cf. Fig. 4). Among type-IV poles shown in (a) and (b), the ones corresponding to the first and second zeros of the Airy functions and their derivatives are exemplified by labeling $l = 1, 2$. (c) and (d) are the magnification of (a) and (b) clarifying type-I, type-II, and type-III poles, separated by the vertical dashed lines of $|\mathrm{Re}(\nu_R)| = \mathrm{Re}(kR)$. Around this border, while RPs of TM polarization continue smoothly, those of TE are strongly pulled upward due to the Brewster angle, which corresponds to a near but slightly lower value of the vertical lines (see text).

$S_{\nu_R} \to \infty$. They are exemplified by open circles in Figs. 5(a) and 5(c) for TM polarization and Figs. 5(b) and 5(d) for TE polarization when $kR = 30$ and $n = 2.4$. The positions of these complex poles and the deformed integral contour enclosing them can be found in Fig. 4.

A. Classification of Regge poles

These singularities are the very RPs and are categorized into four different classes [24–26,61]: (i) type I, highly confined states; (ii) type II, relatively well-confined states; (iii) type III, almost integer values in the second quadrant; and (iv) type IV, creeping wave states. The two former poles (≡IR-RPs) are associated with IRs while the last one (≡ER-RPs) with ERs. Note that a clear interpretation of type-III poles is still missing to the best of our knowledge. To examine the equivalency between ERs and ER-RPs, we obtain the values of m (now, it is $\nu \in \mathbb{C}$) in Fig. 5 by solving Eqs. (6) and (7) for $kR = 30$, $n = 2.4$, and $l = 1, 2, 3, \ldots$. As these values exactly coincide with numerical ones, now it is evident that ERs are indeed the creeping wave modes. Note that numerical Bessel functions with complex orders are computed by using the algorithm recently developed in Ref. [62].

B. Regge trajectories of different polarizations

The energy- (wave-number-) dependent RPs are called Regge trajectories, and they are of critical interest since they

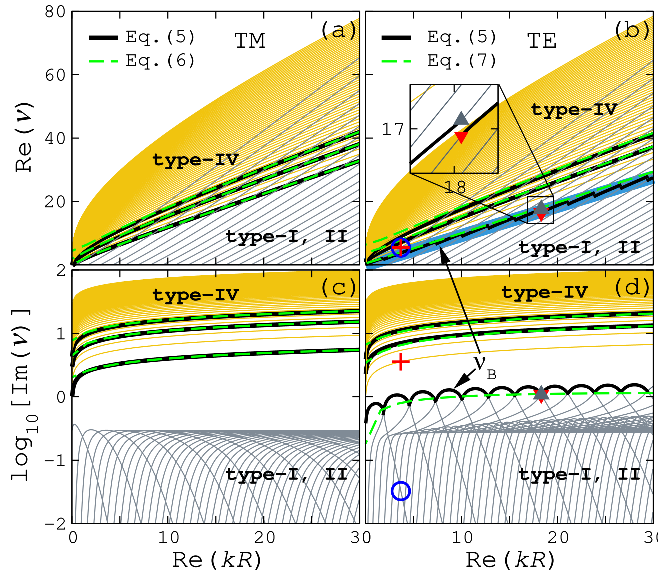

FIG. 6. Real and imaginary parts of RTs obtained numerically by Eq. (5) for TM [(a), (c)] and TE polarization [(b), (d)] when $n = 2.4$. The inset in (b) is the zoom of the avoided crossing between type-II and type-IV poles of Brewster modes. The examples of the strong- and the weak-coupling pairs are respectively marked by the symbols (▲, ▼) and (+, ◯) in (b) and (d). Type-IV poles obtained numerically by Eq. (5) and by Eqs. (6) and (7) for $l = 1$, 4, and 7 are exemplified by the bold solid and bold dashed curves, respectively. All other curves of type I, II, and IV in (a)–(d) are numerically obtained by Eq. (5). The special RTs corresponding to the Brewster mode ν_B in Eq. (12) are indicated by the arrows in (b) and (d).

deliver crucial information on the distinctive characteristics of different types of RPs [24–26,30]. Typically, ER-RPs converge to "zero" as $kR \to 0$, while IR-RPs to the negative real-valued integers, via type-III RPs. We have confirmed that this prediction is concretely valid in our case as well, and the partial structure of RTs in the first quadrant is shown in Fig. 6. In the figure, the clear agreement between RTs computed numerically and by Eqs. (6) and (7) is affirmed once again. Despite the fact that the agreement between the asymptotic expressions in Eqs. (6) and (7) and the numerical solutions of Eq. (5) is already evident, to demonstrate the explicit functional form of RPs in terms of kR and $n > 0$, we derive them as follows:

$$\nu^{R\text{-TM}}_{l,kR} \approx \nu^{\mathrm{TM}}_{\mathrm{PEC}} + \delta_{\mathrm{TM}} \approx kR + c_l (kR)^{\frac{1}{3}} + d_l (kR)^{-\frac{1}{3}} + \frac{i}{\sqrt{n^2-1}} + \frac{2^{-3}\left(5 + 2^5 c_l^3\right)}{c_l\left(1 - 4\sqrt{2}c_l^{\frac{3}{2}}\right)\left(n^2-1\right)} (kR)^{-\frac{1}{3}}, \quad (10)$$

$$\nu^{R\text{-TE}}_{l,kR} \approx \nu^{\mathrm{TE}}_{\mathrm{PEC}} + \delta_{\mathrm{TE}} \approx kR + c_l (kR)^{\frac{1}{3}} + d_l (kR)^{-\frac{1}{3}} + \frac{i2^4 c_l^3}{\left(5 + 2^5 c_l^3\right) n^2 \sqrt{n^2-1}} - \frac{i2^4 c_l^2 \sqrt{n^2-1}}{\left(5 + 2^5 c_l^3\right) n^2} (kR)^{\frac{2}{3}}. \quad (11)$$

Here, the coefficient is given as $c_l = q_l e^{i\pi/3}/2^{1/3}$ and $d_l = q_l^2 e^{2i\pi/3}/(2^{5/3}15)$, where q_l is the lth zeros of the Airy function of the first kind, $\mathrm{Ai}(-q_l) = 0$ for TM polarization, and $c_l = q_l e^{i\pi/3}/2^{1/3}$ and $d_l = e^{2i\pi/3}[2^{1/3}/q_l + q_l^2/(2^{2/3}3)]/10$, where q_l is the lth zeros of the derivative of the Airy function of the first kind, $\mathrm{Ai}'(-q_l) = 0$ for TE polarization, respectively. Again, each of the first three terms on the RHS in Eqs. (10) and (11), respectively, stand for the angular momentum zeros of the Hankel function of the first kind and their derivatives for fixed kR, $H^{(1)}_{\nu^{\mathrm{TM}}_{\mathrm{PEC}}}(kR) = 0$ and $H'^{(1)}_{\nu^{\mathrm{TE}}_{\mathrm{PEC}}}(kR) = 0$ [57,63], while the remaining terms correspond to the dielectric corrections $\delta_{\mathrm{TM/TE}}$. The essential deriving procedures are all the same as before in obtaining Eqs. (6) and (7), but differently for ν (or m), i.e., around the zeros of the angular momentum m, not kR.

Deforming the integral contour to include RPs and to exclude the normal poles (see Fig. 4), we can reproduce the same scattering cross section which was previously given by Eq. (4). Taking into account the contribution of RPs together with that of the background integral [61,64], which asymptotically converges to $\sigma_g/R \equiv 2 \times (2R)/R$ as $kR \to \infty$ (extinction paradox [61,65–70]), the excellent reproduction is found in Fig. 2. Although some small discrepancies arising due to the numerical instability, e.g., of Bessel functions expressed in terms of complex angular momenta, are observed in Fig. 2, still, their overall agreement is reasonably good. Note that the contour deformation does not have a prior fixed form and is selected differently according to the given circumstances [61,71,72].

After a more careful inspection of RTs, it is revealed that there are additional special RPs of type IV in the TE case differently from the TM case. These special RPs ($\equiv$Brewster-RPs) are related to the Brewster angle $\theta_{\mathrm{B}} = \sin^{-1}[1/(1+n^2)^{1/2}]$ and can be approximated through the semiclassical relation $\mathrm{Re}[\nu_B] \approx nk_BR\sin\theta_{\mathrm{B}}$ [20] as

$$\mathrm{Re}[\nu_B] \approx k_BR/\sqrt{1+n^{-2}}. \tag{12}$$

The thick curves in Figs. 3(b) and 6(b) respectively show k_BR and ν_B for $n = 2.4$. Since these curves coincide with those of Eq. (7) [and (11); not shown to avoid overflow information of the figure] for $l = 1$, it turns out that the first ER-RP for TE polarization is associated with the Brewster angle. It should be emphasized that the first ER-RPs, i.e., the lowest damping pole having the smallest absolute value of the imaginary part of the poles, are the most crucial ones [43–46]. In general, they are nicely approximated by zeros of the Airy function at $|\nu| \approx |kR|$, such that $|\nu - kR| \ll |kR|^{1/3}$ [25,27–29]. Taking the first two terms in Eq. (10) or (11) depending on the considered polarization, we can obtain the explicit form of the real and imaginary parts of ER-RPs, as follows:

$$\nu_l \approx kR + \frac{(kR)^{\frac{1}{3}}}{2^{\frac{4}{3}}}q_l + i\left(\frac{1}{\sqrt{n^2-1}} + \frac{\sqrt{3}}{2}q_l\right), \tag{13}$$

where $q_l \in \mathbb{R}$ is the lth zero of the Airy function of the first kind, $\mathrm{Ai}(-q_l) = 0$ for TM polarization and the derivative of it, $\mathrm{Ai}'(-q_l) = 0$ for TE polarization. Since the imaginary part of ν_l grows as q_l increases for fixed values of $\{kR, n\} \in \mathbb{R}$, the lowest damping pole corresponds to the first, i.e., $l = 1$, zero of the Airy function of the first kind and its derivative, i.e., $\mathrm{Ai}(-q_1) = 0$ and $\mathrm{Ai}'(-q_1) = 0$. These poles are the ones near the critical angle, $\theta_c = \sin^{-1}[1/n]$ [61,73]. However, as our results indicate, it turns out that the first ER-RPs in the TE case are Brewster-RPs near the Brewster angle that $\theta_{\mathrm{B}} \neq \theta_c$.

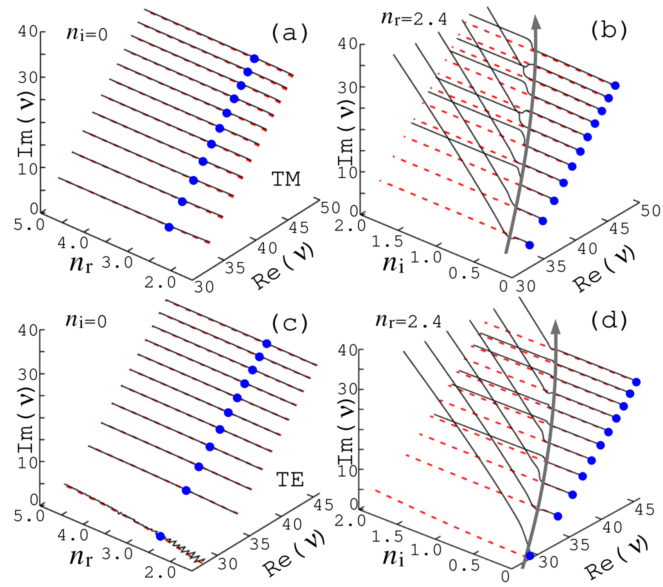

FIG. 7. Type-IV RPs for TM [(a), (b)] and TE [(c), (d)] polarization as functions of a complex-valued refractive index, $n = n_r + in_i$, for which $\{n : 1.5 \leqslant n_r \leqslant 5, n_i = 0\}$ in (a) and (c), and $\{n : n_r = 2.4, 0 \leqslant n_i \leqslant 2\}$ in (b) and (d). The thin solid curves are obtained numerically by Eq. (5) and the thin dashed ones analytically by Eqs. (10) and (11), respectively. The solid circles (•) mark type-IV RPs, which are the same ones previously shown in Figs. 5(a) and 5(b). Due to the occurrence of interactions among RPs, Eqs. (10) and (11) fail to reproduce the numerical results on the left-hand side of the arrowed curves in (b) and (d), as the imaginary part of the refractive index increases. Note, for the same reason, as $n_r \to 1$, a relatively large (but still in good agreement) discrepancy between the numerical results and Eqs. (10) and (11) of the first ER-RP for TE is observed in (c).

To demonstrate the general applicability of Eqs. (10) and (11) for a different material property, i.e., different values of the refractive index, we obtain ER-RPs as a function of the refractive index in Fig. 7. In Figs. 7(a) and 7(c), we can confirm the robust agreement between the numerical results obtained by Eq. (5) and the analytic ones by Eqs. (10) and (11) over a wide range of the refractive index, when the imaginary part of the refractive index is set to zero (i.e., a general passive medium without accountable absorption or pumping). On the other hand, it turns out that when a nonzero imaginary part of the refractive index is introduced, strong deviations between the numerical and the analytic calculations are brought about, as this imaginary part increases [see Figs. 7(b) and 7(d)]. Since it was proven that the internal-external mode interactions in the $kR \in \mathbb{C}$ plane could rather easily take place when the refractive index has a nonzero imaginary value [19], we can attribute this large deviation to the interactions among RPs, particularly between IR-RPs and ER-RPs. In other words, as the imaginary part of the refractive index increases, ER-RPs can couple with IR-RPs at the specific value, and because some of the ER-RPs turn into IR-RPs after this interaction, they do not follow Eqs. (10) and (11), which are derived for ER-RPs. Nevertheless, we can confirm the concrete validity of Eqs. (10) and (11) before those interactions take place, as we can see on the right-hand side of the arrowed curves in Figs. 7(b) and 7(d).

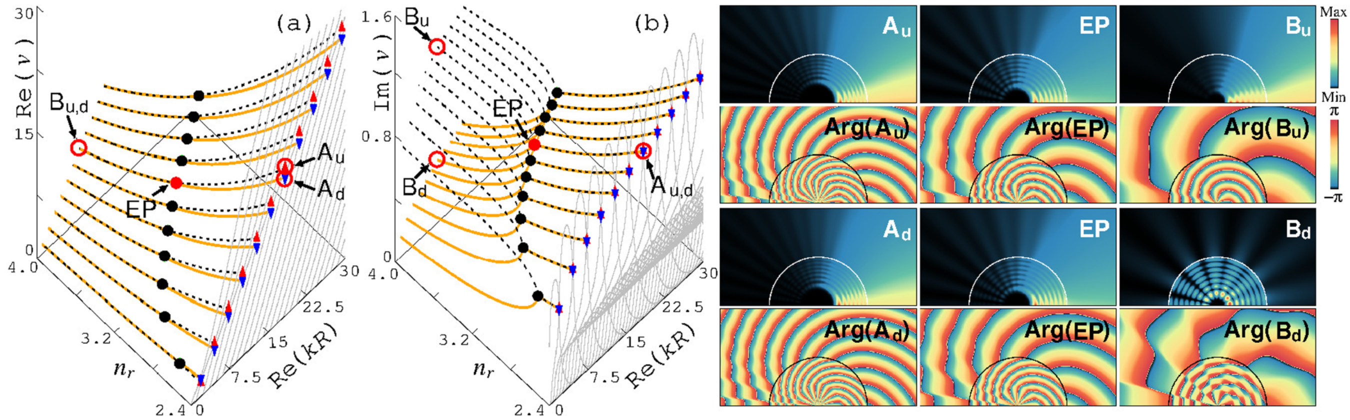

FIG. 8. (a) Real and (b) imaginary parts of RPs for the TE polarization as functions of $[\mathrm{Re}(kR), n_r]$, where $n_r \in \mathbb{R}$ is the real part of the refractive index with a fixed imaginary part $n_i = 0$. EPs at which IR-RPs (thick solid) and Brewster-RPs (thick dashed) coalesce are marked by solid circles (•). RTs for $n_r = 2.4$ are given by thin gray curves, and the strong-coupling pairs are marked by pairs of symbols (▲, ▼). Intensities and phases [Arg(·)] of the selected wave functions corresponding to poles marked by $A_{u,d}$, $B_{u,d}$, and EP in (a) and (b) are examined in the right-hand panels with the same labels.

V. NON-HERMITIAN DEGENERACY OF REGGE POLES

As a final remark, we clarify the emergence of EPs in RPs. To this end, we compute all RPs directly by numerically solving Eq. (5). In Figs. 6(b) and 6(d), we can see several consecutive interactions between Brewster-RPs and IR-RPs exhibiting strong couplings: avoided crossings in $\mathrm{Re}[\nu_R]$ and crossings in $\mathrm{Im}[\nu_R]$. As the real part of the refractive index increases, these couplings switch into weak ones: avoided crossings in $\mathrm{Im}[\nu_R]$ and crossings in $\mathrm{Re}[\nu_R]$. The transition point of the two coupling regimes is EP at which $\mathrm{Re}[\nu_R]$ and $\mathrm{Im}[\nu_R]$ coalesce simultaneously. The branch cut curves over those coupling regimes in the Riemann surface in Fig. 8 reveal clear second-order EPs for several pairs of RPs. In the figure, the wave functions for the poles in the weak- and strong-coupling regimes are obtained by applying Eq. (8) to Eq. (1). A coalescence of the wave functions at EP is transparently demonstrated by their identical phase plots in the figure. On the other hand, typical pairs of ER-RPs and IR-RPs are initially in the weak-coupling regime and transit to the strong one via EPs, when the imaginary part of the refractive index increases, as shown in Figs. 9(a) and 9(b). It is emphasized that the overall transitions across the strong and weak couplings of pairs of IR-RPs and ER-RPs are general phenomena regardless of the polarization, although we have focused on the TE case just to deal with the special Brewster-RPs. The exemplifying lowest ten parameter values obtained for EPs coalescing two different pairs of RPs are summarized in Table I: Pair-A ←Brewster-RPs and IR-RPs; Pair-B ←general ER-RPs and IR-RPs.

VI. CONCLUSION

Through our findings presented so far, it has been proven that a surface creeping wave is the nature of ERs and can form EPs. Despite the focus of the present works having been mainly on optical microdisks, we believe our conclusions can

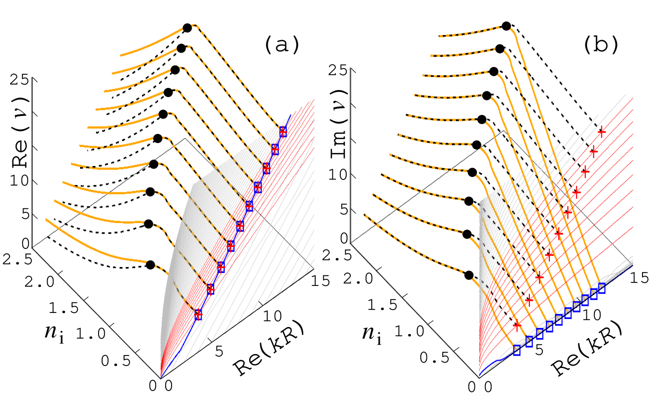

FIG. 9. (a) Real and (b) imaginary parts of RPs for the TE polarization as functions of $[\mathrm{Re}(kR), n_i]$, where $n_i \in \mathbb{R}$ is the imaginary part of the refractive index for a fixed real part $n_r = 2.4$. EPs at which IR-RPs (thick solid) and ER-RPs (thick dashed) coalesce are marked by solid circles (•). RTs for $n_i = 0$ are given by thin gray curves, and the weak-coupling pairs are marked by pairs of symbols (+, □).

TABLE I. Sets of the parameter values $[n_r, n_i; \mathrm{Re}(kR)]$ for EPs coalescing (Pair A) Brewster-RPs and IR-RPs and (Pair B) general ER-RPs and IR-RPs. The parameter values of pair A correspond to EPs marked by solid circles (•) in Fig. 8, and the ones of pair B correspond to EPs marked by solid circles (•) in Fig. 9, respectively.

	Pair A			Pair B		
Index	n_r	n_i	Re(kR)	n_r	n_i	Re(kR)
1	2.609	0.0	1.683	2.4	0.942	3.733
2	2.857	0.0	3.483	2.4	1.231	4.996
3	2.975	0.0	5.172	2.4	1.407	6.055
4	3.053	0.0	6.792	2.4	1.533	7.030
5	3.106	0.0	8.393	2.4	1.633	7.933
6	3.145	0.0	9.974	2.4	1.709	8.846
7	3.171	0.0	11.567	2.4	1.771	9.674
8	3.197	0.0	13.119	2.4	1.822	10.585
9	3.223	0.0	14.631	2.4	1.872	11.441
10	3.249	0.0	16.105	2.4	1.910	12.265

be extended immediately to the extensive other physical systems. More importantly, we expect that our results shed light on various aspects of scattering and resonant problems related to openness. Therefore, we hope to settle many puzzling phenomena in the fields of non-Hermitian quantum chaos by understanding more deeply the surface creeping waves propagating around the noncircular boundaries of chaotic systems. To start, we would deal with the effects of surface creeping waves on quantum or wave states in classically chaotic systems in the future.

[1] M.-A. Miri and A. Alù, Science **363**, eaar7709(2019).
[2] L. Feng, R. El-Ganainy, and L. Ge, Nat. Photonics **11**, 752 (2017).
[3] R. El-Ganainy, K. G. Makris, M. Khajavikhan, Z. H. Musslimani, S. Rotter, and D. N. Christodoulides, Nat. Phys. **14**, 11 (2018).
[4] H. Cao and J. Wiersig, Rev. Mod. Phys. **87**, 61 (2015).
[5] J. Wiersig, Phys. Rev. Research **1**, 033182 (2019).
[6] S. H. Schot, Hist. Math. **19**, 385 (1992).
[7] T. Kato, *Perturbation Theory for Linear Operators* (Springer, New York, 1966).
[8] W. D. Heiss, Phys. Rev. E **61**, 929 (2000).
[9] M. V. Berry, Czech. J. Phys. **54**, 1039 (2004).
[10] C. Dembowski, H.-D. Gräf, H. L. Harney, A. Heine, W. D. Heiss, H. Rehfeld, and A. Richter, Phys. Rev. Lett. **86**, 787 (2001).
[11] B. Peng, Ş. K. Özdemir, M. Liertzer, W. Chen, J. Kramer, H. Yilmaz, J. Wiersig, S. Rotter, and L. Yang, Proc. Natl. Acad. Sci. USA **113**, 6845 (2016).
[12] W. Chen, Ş. Kaya Özdemir, G. Zhao, J. Wiersig, and L. Yang, Nature (London) **548**, 192 (2017).
[13] C.-H. Yi, J. Kullig, and J. Wiersig, Phys. Rev. Lett. **120**, 093902 (2018).
[14] J. Kullig, C.-H. Yi, M. Hentschel, and J. Wiersig, New J. Phys. **20**, 083016 (2018).
[15] J. Kullig and J. Wiersig, Phys. Rev. A **100**, 043837 (2019).
[16] J. Ryu, S. Gwak, J. Kim, H.-H. Yu, J.-H. Kim, J.-W. Lee, C.-H. Yi, and C.-M. Kim, Photonics Res. **7**, 1473 (2019).
[17] C. P. Dettmann, G. V. Morozov, M. Sieber, and H. Waalkens, Europhys. Lett. **87**, 34003 (2009).
[18] J. Cho, S. Rim, and C.-M. Kim, Phys. Rev. A **83**, 043810 (2011).
[19] C.-H. Yi, J. Kullig, M. Hentschel, and J. Wiersig, Photonics Res. **7**, 464 (2019).
[20] J. U. Nöckel, Resonances in nonintegrable open systems, Ph.D. thesis, Yale University, 1997.
[21] T. Harayama and S. Shinohara, Laser Photonics Rev. **5**, 247 (2011).
[22] C. A. Valagiannopoulos, Prog. Electromagn. Res. **75**, 137 (2007).
[23] H. C. van de Hulst, *Light Scattering by Small Particles* (Courier Corporation, North Chelmsford, MA, 1981).
[24] H. M. Nussenzveig, Ann. Phys. **34**, 23 (1965).
[25] H. M. Nussenzveig, J. Math. Phys. **10**, 82 (1969).
[26] H. M. Nussenzveig, J. Math. Phys. **10**, 125 (1969).
[27] A. Ishimaru, *Electromagnetic Wave Propagation, Radiation, and Scattering: From Fundamentals to Applications* (Wiley, Hoboken, NJ, 2017).
[28] A. V. Osipov and S. A. Tretyakov, *Modern Electromagnetic Scattering Theory with Applications* (Wiley, Hoboken, NJ, 2017).
[29] D. Colton and R. Kress, *Inverse Acoustic and Electromagnetic Scattering Theory*, Vol. 93 (Springer, Berlin, 2012).
[30] T. Regge, Nuovo Cimento **14**, 951 (1959).
[31] N. A. Logan, Proc. IEEE **53**, 773 (1965).
[32] H. M. Nussenzveig, *Diffraction Effects in Semiclassical Scattering*, Vol. 1 (Cambridge University Press, Cambridge, UK, 2006).
[33] A. Bottino, Acc. Sc. Torino, Atti Sc. Fis. **152**, 61 (2018).
[34] G. F. Chew and S. C. Frautschi, Phys. Rev. Lett. **8**, 41 (1962).
[35] G. N. Watson, Proc. R. Soc. London, Ser. A **95**, 83 (1918).
[36] A. Tijhuis, IEEE Trans. Antennas Propag. **34**, 813 (1986).
[37] C.-C. Chen, IEEE Trans. Antennas Propag. **46**, 1074 (1998).
[38] J. Bros and G. Viano, Ann. Henri Poincaré **1**, 101 (2000).
[39] E. De Micheli and G. A. Viano, Ann. Phys. (NY) **323**, 1817 (2008).
[40] S. R. Dolan, L. A. Oliveira, and L. C. B. Crispino, Phys. Rev. D **82**, 084037 (2010).
[41] H. Überall, Diffusion et Diffraction **2**, 353 (1985).
[42] H. Überall, *Acoustic Resonance Scattering* (CRC Press, Boca Raton, FL, 1992).
[43] A. Folacci and M. Ould El Hadj, Phys. Rev. D **99**, 104079 (2019).
[44] A. Folacci and M. Ould El Hadj, Phys. Rev. D **100**, 064009 (2019).
[45] A. Folacci and M. Ould El Hadj, Phys. Rev. D **98**, 064052 (2018).
[46] M. Ould El Hadj, T. Stratton, and S. R. Dolan, Phys. Rev. D **101**, 104035 (2020).
[47] S. Ancey, Y. Décanini, A. Folacci, and P. Gabrielli, Phys. Rev. B **70**, 245406 (2004).
[48] S. Ancey, Y. Décanini, A. Folacci, and P. Gabrielli, Phys. Rev. B **76**, 195413 (2007).
[49] K. V. Protasov and A. Y. Voronin, Adv. High Energy Phys. **2014**, 124592 (2014).
[50] D. Sokolovski, Z. Felfli, S. Y. Ovchinnikov, J. H. Macek, and A. Z. Msezane, Phys. Rev. A **76**, 012705 (2007).
[51] Y. Décanini and A. Folacci, Phys. Rev. A **67**, 042704 (2003).
[52] W. Wang, L. Yang, Q. Zhang, and T. Jiang, IEEE J. Sel. Areas Commun. **36**, 696 (2018).
[53] P. Cao and J. H. Wu, J. Appl. Phys. **121**, 105103 (2017).
[54] R. Dubertrand, E. Bogomolny, N. Djellali, M. Lebental, and C. Schmit, Phys. Rev. A **77**, 013804 (2008).
[55] E. Bogomolny, R. Dubertrand, and C. Schmit, Phys. Rev. E **78**, 056202 (2008).
[56] J. B. Keller, S. Rubinow, and M. Goldstein, J. Math. Phys. **4**, 829 (1963).
[57] A. Wirzba, Phys. Rep. **309**, 1 (1999).
[58] L. B. Felsen and N. Marcuvitz, *Radiation and Scattering of Waves*, Vol. 31 (Wiley, New York, 1994).
[59] A. Cruz and J. Sesma, Math. Comput. **39**, 639 (1982).

[60] J. W. Brown, R. V. Churchill *et al.*, *Complex Variables and Applications* (McGraw-Hill, Boston, 2009).
[61] J. A. Adam, Phys. Rep. **356**, 229 (2002).
[62] M. Kodama, ACM Trans. Math. Softw. **37**, 1 (2011).
[63] W. Franz and R. Galle, Z. Naturforsch., A **10**, 374 (1955).
[64] J. Connor, J. Chem. Phys. **138**, 124310 (2013).
[65] M. J. Berg, C. Sorensen, and A. Chakrabarti, J. Quant. Spectrosc. Radiat. Transfer **112**, 1170 (2011).
[66] H. Lai, W. Wong, and W. Wong, J. Opt. Soc. Am. A **21**, 2324 (2004).
[67] J. A. Lock, J. Opt. Soc. Am. A **12**, 929 (1995).
[68] E. W. Montroll and R. W. Hart, J. Appl. Phys. **22**, 1278 (1951).
[69] L. Brillouin, J. Appl. Phys. **20**, 1110 (1949).
[70] P. Morse and H. Feshbach, *Methods of Theoretical Physics*, International Series in Pure and Applied Physics Vol. 2 (McGraw-Hill, New York, 1953), pp. 1380–1381.
[71] E. Spence, The Watson Transformation Revisited, 2012 (unpublished).
[72] R. G. Newton, *Scattering Theory of Waves and Particles* (Springer, Berlin, 2013).
[73] N. Fiedler-Ferrari and H. M. Nussenzveig, Part. Part. Syst. Charact. **4**, 147 (1987).